LETTERS
https://doi.org/10.1038/s41565-017-0030-x
nature nanotechnology

Electrical control of charged carriers and excitons in atomically thin materials

Ke Wang[1], Kristiaan De Greve[1,2], Luis A. Jauregui[1], Andrey Sushko[1], Alexander High[1,2], You Zhou[1,2], Giovanni Scuri[1], Takashi Taniguchi[3], Kenji Watanabe[3], Mikhail D. Lukin[1], Hongkun Park[1,2] and Philip Kim[1]*

Electrical confinement and manipulation of charge carriers in semiconducting nanostructures are essential for realizing functional quantum electronic devices[1–3]. The unique band structure[4–7] of atomically thin transition metal dichalcogenides (TMDs) offers a new route towards realizing novel 2D quantum electronic devices, such as valleytronic devices and valley–spin qubits[8]. 2D TMDs also provide a platform for novel quantum optoelectronic devices[9–11] due to their large exciton binding energy[12,13]. However, controlled confinement and manipulation of electronic and excitonic excitations in TMD nanostructures have been technically challenging due to the prevailing disorder in the material, preventing accurate experimental control of local confinement and tunnel couplings[14–16]. Here we demonstrate a novel method for creating high-quality heterostructures composed of atomically thin materials that allows for efficient electrical control of excitations. Specifically, we demonstrate quantum transport in the gate-defined, quantum-confined region, observing spin–valley locked quantized conductance in quantum point contacts. We also realize gate-controlled Coulomb blockade associated with confinement of electrons and demonstrate electrical control over charged excitons with tunable local confinement potentials and tunnel couplings. Our work provides a basis for novel quantum opto-electronic devices based on manipulation of charged carriers and excitons.

In TMD semiconductors, the in-plane hexagonal lattice structure with two inequivalent lattice sites generates band edges near the corner of the Brillouin zone, known as K(Q) and K′(Q′) valleys for monolayers and trilayers, respectively[4–7,17–19]. In these odd-numbered atomically thin TMDs, the broken inversion symmetry of the lattice, in combination with the strong spin–orbit interaction, polarizes spins in opposite directions at each valley. This locked spin–valley degree of freedom, together with the large exciton binding energy[11], has been proposed as the key ingredient in a number of novel quantum electronic and optoelectronic structures[8,12,14,20,21].

The first step towards quantum manipulation of electrons and charged excitons is to demonstrate charge confinement with tunable confinement potentials and tunnel couplings in atomically thin TMDs[1–3]. Previously, quantum dots have been demonstrated in quasi-2D TMDs (more than seven atomic layers) in top-gated WSe_2 and WS_2 on a SiO_2 substrate[15,16]. However, in these thicker TMDs, the bandgap becomes indirect and spin–orbit gaps become smaller, making them not well suited for valleytronics and optoelectronic applications. In addition, the residual disorder limits the mobility and device homogeneity, preventing accurate experimental control over local confinement and tunnelling couplings in these devices, which are crucial for qubit preparation[1–3]. The resulting inhomogeneous two-dimensional electron gases (2DEGs) can lead to accidental quantum dot (QD) formation dominated by disorder, with significantly reduced device controllability, similar to those identified in mesoscopic quantum devices including modulation-doped Si/SiGe QDs[22], short MoS_2 channels[14] and graphene nanoribbons[21,23].

It is well known that achieving homogeneous 2DEG and transparent ohmic contacts become drastically more difficult as the thickness of a TMD approaches the atomic limit[24–26]. To overcome these challenges, we employ a van der Waals (vdW) heterostructure consisting of hBN/MoS_2/hBN with graphene contacts, assembled using a dry transfer technique[27] (Fig. 1a) in controlled environment, followed by low-temperature illumination (see Supplementary Information). The resulting vdW heterostructure consists of two pieces of graphene providing electrical contacts to a piece of intrinsic MoS_2 channel (trilayer), which are then encapsulated in hBN (60–80 nm). The choice of a MoS_2 trilayer instead of a monolayer sample is to maximize the contact transparency necessary for the QD operation, while preserving the broken inversion symmetry necessary for the spin–valley locked band edges found at the Q valleys with a spin–orbit gap comparable to monolayers[19] (see Supplementary Information).

The mean free path of carriers is characterized to be ~100 nm (see Supplementary Information), thus the local gate structure whose characteristic size is ~50 nm should provide quantum confinement by charging the local gates. In addition, the contact barrier is characterized to be lower than the order of 0.1 meV, allowing transport study of the quantized levels. We first discuss the configuration where all local gates are tied together to the same potential V_{local} (Fig. 2a). In this configuration, the current flows through gate-defined constrictions known as quantum point contacts (QPCs)[28]. In TMD QPCs, quantized conductance in steps of $12e^2/h$ is expected considering the twofold spin degeneracy and sixfold Q valley degeneracy[19]. Fig. 2a shows the measured current across the device as a function of back-gate (V_{BG}) and local-gate (V_{local}) voltages with a 1 mV alternating current bias (zero d.c. bias). As the carrier density becomes higher at more positive V_{BG}, the electrostatic pinch-off of the channel happens at more negative V_{local}, (with high on–off ratios of the conductance of more than 10^6). 1D sweeps of V_{local} at several fixed back-gate voltages exhibit plateau-like features (Fig. 2b), a consequence of conductance quantization in the QPC as the channel width becomes comparable to the Fermi wavelength[28]. Due to the comparably lower channel mobility and contact quality

[1]Department of Physics, Harvard University, Cambridge, MA, USA. [2]Department of Chemistry and Chemical Biology, Harvard University, Cambridge, MA, USA. [3]National Institute for Materials Science, Namiki 1-1, Ibaraki, Japan. *e-mail: pkim@physics.harvard.edu

© 2018 Macmillan Publishers Limited, part of Springer Nature. All rights reserved.

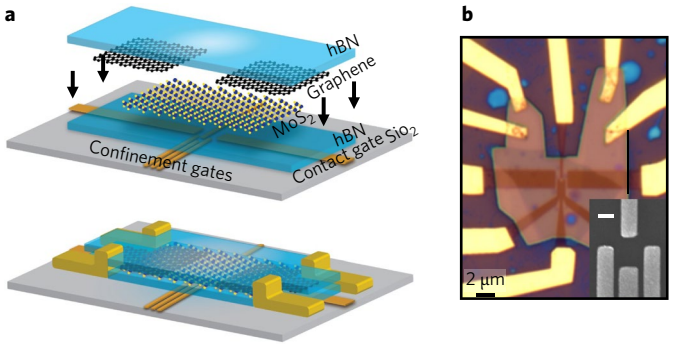

Fig. 1 | Semiconducting van der Waals heterostructure with mesoscopic backgates. a, The van der Waals heterostructure consists of two hBN flakes (~60–80 nm), two single-layer graphene flakes and one trilayer MoS_2 flake. The stack has been assembled and transferred on top of the pre-patterned local confinement and contact gates, using the dry-transfer technique. Subsequently, Cr/Pd/Au edge contacts are made to graphene flakes, making van der Waals electrical contact to the MoS_2 channel. **b**, Optical microscope image of the gate-defined QD device. The inset shows an SEM image of the local confinement gates. Inset scale bar, 200 nm. Graphene contacts to MoS_2 are improved by positively biased local contact gates, while the quantum confinement in the QD is defined by negatively biased local fine gates.

of the trilayer MoS_2 2DEG (compared with those of Si and GaAs counterparts), the two-probe conductance we measure across the QPC contains a significant contribution from contact resistances and the bulk 2DEG series channel resistance leading to the QPC. Assuming the first plateau of conductance appears at $12e^2/h$, we can estimate this series resistance contribution R_0. The inset of Fig. 2b shows R_0 at different values of V_{BG}, where it is typically tens of kΩs and decreases with increasing V_{BG}, consistent with our measurements on contact resistances from the Hall bars fabricated in a similar way (Supplementary Fig. 1). We also note that at higher overall electron density (higher V_{BG}), the last plateau tends to gradually split into two with increasing 2DEG density, suggesting that the valley–spin locked band edges are energetically resolved locally due to enhanced screening from charge inhomogeneity. Further improvement of the 2DEG and electrical contact quality as well as optimization of device geometry (4-probe, Supplementary Fig. 2a) are required to demonstrate exact quantization, which may provide better insight into the valley–spin locked band edges.

It is important to note that the conductance of the device shown in Fig. 2 exhibits a monotonic increase as a function of both V_{BG} and V_{QPC}. This observation is in sharp contrast to 'accidental' QD formation due to the disorder landscape, where rapid Coulomb oscillations are observed over a wide range of gate parameters. Such behaviour is due to the disorder-defined tunnel couplings, which are insensitive to applied gate voltages (Supplementary Fig. 2b). The monotonic control of each QPC channel achieved in our gate-defined QDs enables us to precisely tune the QD–reservoir-tunnel couplings. Figure 3a shows the measured current across the device as a function of V_L and V_R at fixed centre gate voltages $V_N = -8$ V and $V_C = -10$ V. The conducting region is in a rectangular shape located at the upper right corner of the V_R–V_L diagram, with plateau locations depending only on a single (left or right) gate voltage: this observation demonstrates that the left (right) tunnel coupling can be independently tuned by V_L (V_R) as we designed. Near the lower-left corner of the conducting region (white dashed box), we found a suitable gate range where both tunnel couplings are optimized such that the tunnel-broadening of quantized levels in the dot becomes smaller than the charging energy E_C, while the current across device remains above the measurement threshold (~1 pA).

With independent control of tunnel couplings, we now demonstrate single-electron transistor (SET) operation of our TMD device. Figure 3b shows a detailed gate sweep in the region where we observe multiple regular oscillations of current across the device. Here, when the energy level of the quantum dot is in resonance with the Fermi energy, a finite tunnel current is measured. When no level is in resonance, the device is in the Coulomb blockade regime and current vanishes. The resonant condition is satisfied along negative slope lines in the V_L versus V_R parameter space, the slopes of which correspond to the ratio of their capacitive coupling to the QD, and whose separation is proportional to the charging energy E_C. The observation that the slope and the separation stay relatively constant over many consecutive charge transitions implies that the QD is uniformly defined. The slope of these transition lines is on the order of one, implying the resulting QD is located near the centre of the device. We emphasize that these demonstrations are important metrics to differentiate the origin of the QD formation. If the QDs were accidentally formed due to disorder in 2DEG, the narrowest constriction in the device, that is, the QPC channels, would be a likely place. As a result, the resonant tunnelling lines would appear horizontal or vertical in a V_L versus V_R sweep, since the capacitive couplings to the QDs are dominated by the gates that are defining the QPC channels (Supplementary Fig. 3c). In contrast, in a QD defined in a uniform 2DEG, Coulomb blockade is observed in a much narrower range of gate parameters. Here, the device can be sensitively tuned from the tunnel-broadened regime (triangle in Fig. 3b) to the thermally broadened regime (hexagon in Fig. 3b) over small changes in gate voltages.

The charging energy of the QD can be measured by performing transport spectroscopy at a finite bias voltage V_{SD}. Figure 3c shows the current as a function of V_{SD} while shifting the QD energy levels with a local gate voltage (ΔV_g). A series of diamond-shaped zero-current regions in this diagram is a clear indication of the Coulomb blockade regime where no QD quantum level exists in the bias window defined by V_{SD}. The charging energy (E_C) determined by the height of the diamond along the V_{SD} axis is ~2 meV, consistent with a dot size of $r \sim 70$ nm (ref. [3]) expected for our gate design. We note that the Fermi energy with respect to the band edge, and the charging energy in the QD are both sufficiently smaller than the spin–orbit gap in trilayer MoS_2 (~4.3 meV)[19], ensuring the spin–valley locked nature of confined charge carriers.

Similar to the charge confinement demonstrated by the gate-defined nanostructure, charged excitons can also be manipulated by gate-defined confinement[12,13]. For manipulation of charged excitons

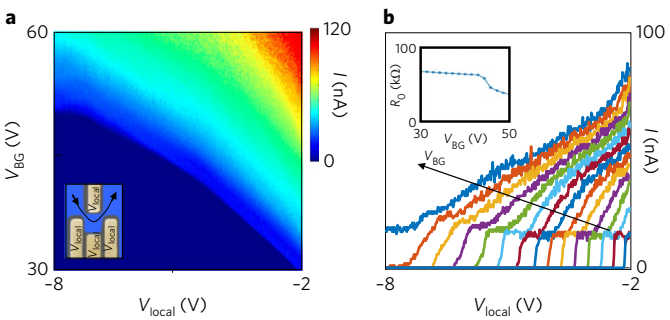

Fig. 2 | Conductance quantization via quantum point contact. a, By energizing the QD gates, two quantum point contact channels can be pinched off over a large range of electron density with a high on/off ratio exceeding 10^6. The conductance changes monotonically, implying a uniform QPC channel with straightforward gate-control. **b**, 1D cuts of the pinch-off curve at various V_{BG} (from 30 V to 52.5 V, with an equidistance step of 1.5 V) reveal development of quantum plateaus, a signature of quantum confinement. The inset shows the series resistance to the QPC estimated from the quantized plateaus.

© 2018 Macmillan Publishers Limited, part of Springer Nature. All rights reserved.

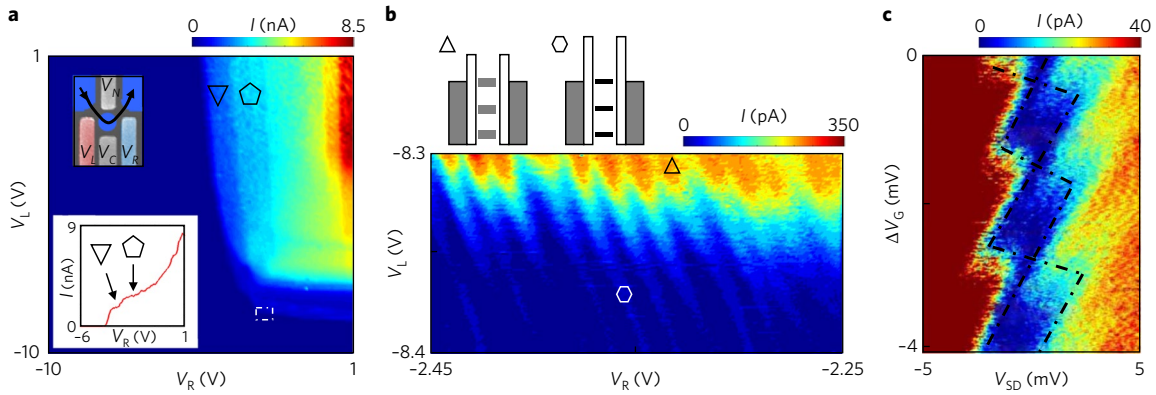

Fig. 3 | Quantum confinement of charge carriers. a, Zero-bias a.c. conductance across the device as a function of left gate voltage V_L and right gate voltage V_R at fixed centre gate voltages $V_N = -8$ V and $V_C = -10$ V. The rectangular shape of the conductance region indicates that the left (right) tunnel coupling getting tuned by V_L (V_R) independently, with visible quantum plateaus (inset). At the corner of the conducting region (dashed box), the tunnel couplings to both the contacts are optimized, so that the levels inside the QD are not significantly broadened by tunnelling. **b**, A zoom-in scan of the boxed region in **a**, revealing a series of resonant tunnelling peaks. The resonant condition is found when the source–drain Fermi level aligns with the quantized levels in the gate-defined QD as shown in the schematic diagram at the top. The symbols correspond to the two different regimes with small (hexagon) and large (uptriangle) tunnelling couplings. The separation and the slope of transitions (~1) stay reasonably constant over more than 10 consecutive charge transitions, implying a uniform dot being established near the centre of the device with well-defined shape and charging energy. By tuning the tunnel couplings with the gate voltages, the quantized levels in the dot can be sensitively tuned from the thermally broadened regime to the tunnel-broadened regime. **c**, A charging energy of ~2 meV and a gate capacitive coupling ratio of ~0.15 can be extracted from the Coulomb diamonds (dashed lines), consistent with electrostatic simulations. Data are extrapolated in order to remove occasional background noise.

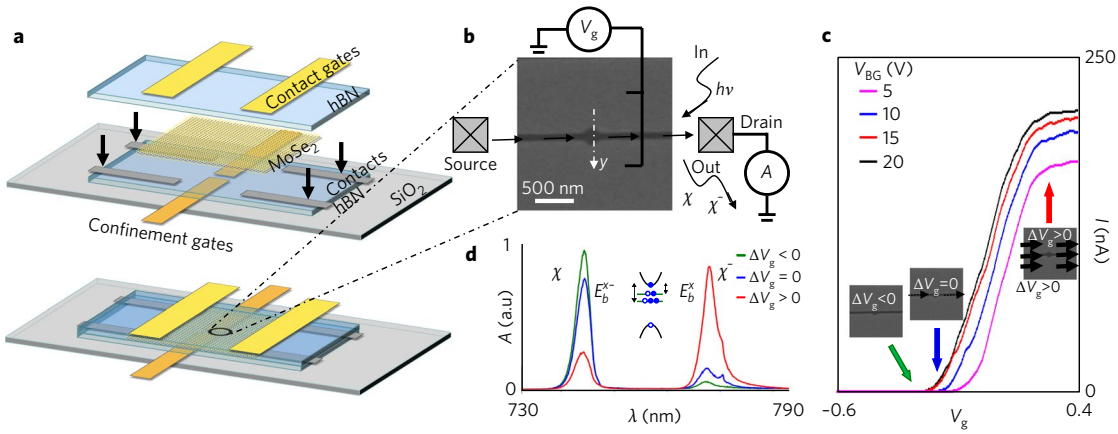

Fig. 4 | Optoelectronic transport in gate-defined $MoSe_2$ nanostructures. a, Local Pt contacts are pre-deposited on the top surface of bottom hBN before the assembly of the van der Waals heterostructure, which consists of two hBN (~60–80 nm) and a piece of mono-layer $MoSe_2$. The stack is then transferred on top of the pre-patterned local confinement gate, using the dry-transfer technique. Subsequently, top Cr/Pd/Au contact gates are deposited for local doping of the contact region. **b**, SEM image of a gate-defined monolayer $MoSe_2$ QD. Current is measured across the channel (black arrowed line), with optical excitation of $\lambda = 660$ nm used to generate neutral excitons (X) and charged excitons (X^-). **c**, Typically measured current across the device as a function of local gate voltage V_g at different silicon backgate voltage V_{BG}. Conductance plateaus are barely visible due to the long length scale of the channel leading to the centre QD, which is required to exceed the laser spot size for well-defined confinement during optical excitation. For ease of discussion, we can define $\Delta V_g = 0$ at the gate configuration where confinement is expected with conductance of the device being near pinch-off (blue arrow for $V_{BG} = 20$ V). Transport across the device happens strictly via tunnelling (thin black arrow) to and from the QD defined in the centre of the device (confinement regime). In contrast, confinement is absent (red arrow) and current (thick black arrows) flow globally across the device at $\Delta V_g > 0.5$ V (accumulation regime), while carriers and therefore currents are globally depleted (green arrow) across the device at $\Delta V_g < -0.2$ V (depletion regime). **d**, Typical re-combination emission signal collected from the device as a function of emission wavelength at different V_g values. The relative ratio between charged (X^-) and neutral exciton (X) recombination emission becomes smaller as V_g becomes more negative and device transits from accumulation regime to confinement regime and depletion regime.

in gate modulated nanostructures, 2D semiconductors, such as TMD monolayers, hold significant advantages over traditional GaAs and Si 2DEGs due to their large exciton binding energy, preventing dissociation of the charged exciton under the influence of electric fields[11,13]. Extending the SET demonstration in atomically thin TMDs discussed above, we now show gate-defined and tunable confinement of charged exciton in 2D TMDs. For optoelectronic confinement demonstration, we chose 2D $MoSe_2$ due to its sharp optical spectrum at low temperatures in comparison to MoS_2 (refs [9–11]). A monolayer sample is essential in this experiment in order to ensure a direct bandgap,

© 2018 Macmillan Publishers Limited, part of Springer Nature. All rights reserved.

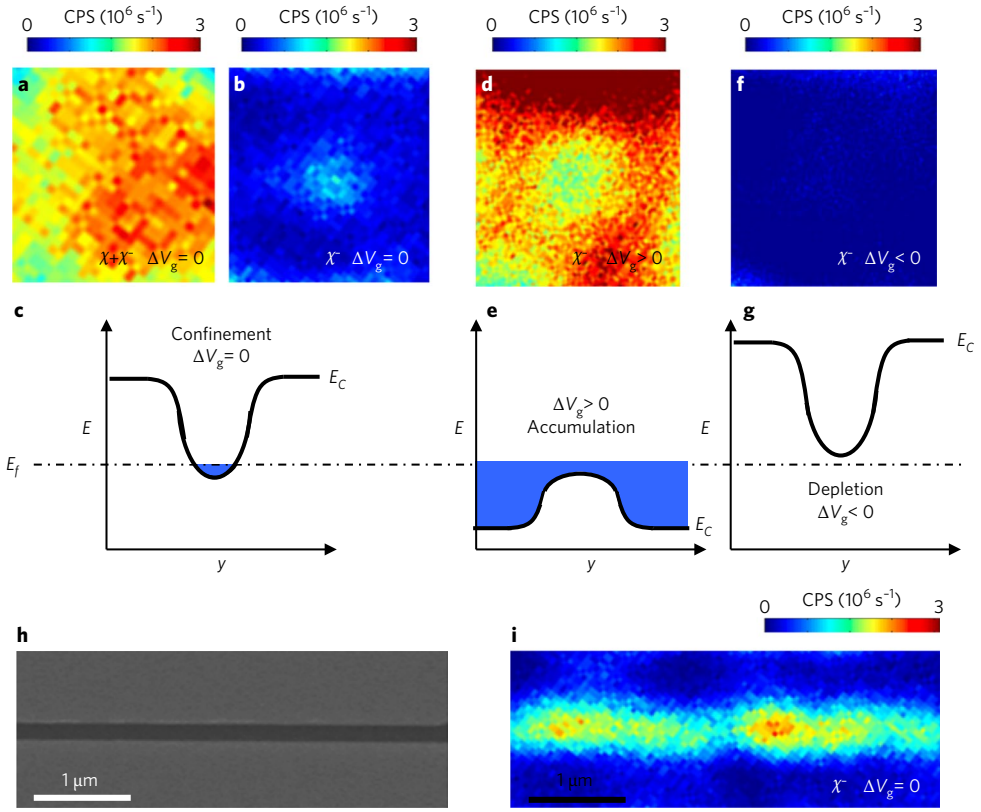

Fig. 5 | Gate-defined confinement of charged excitons. We collect integrated emission signal as a function of laser position, and obtain a spatial map of emission signal in the same region as shown in Fig. 4b. Depending on the range of wavelength we choose, in which the signal are collected and integrated, we obtain an emission map of all excitons (**a**, collected 730–790 nm) and charged excitons only (**b**, collected 760–790 nm) in the depletion regime (**c**). The signal in **a** is dominated by neutral excitons (X), which are delocalized due to their charge-neutral nature, while the charged excitons (X^-) in **b** are electrostatically confined in the centre of the gate-defined quantum well. **d**–**g**, Furthermore, the confinement potential can be sensitively manipulated with local gate voltages to achieve delocalization (**d**,**e**, $\Delta V_g > 0$ V) and depletion (**f**,**g**, $\Delta V_g < 0$ V) of the charged excitons. **c**,**e**,**g**, Energy of conduction band minima E_C along the white dashed line in Fig. 4b demonstrate the expected charge distribution in the device in the three regimes accordingly. **h**,**i**, SEM image (**h**) and charged exciton map (**i**) in a gate-defined 1D channel device at $\Delta V_g = 0$, in which 1D confinement of trions is demonstrated with a wider confinement potential design. Although the confinement is dominated by the gate-defined electrostatic potential, the slight spatial variation of the 1D exciton wire width is a good measure of inhomogeneities in the 2DEG. CPS, counts per second.

necessary for efficient optical excitation and emission. In addition, the local confinement gates (Fig. 4b) are designed to be significantly wider than the diffraction-limited laser spot size (<1 μm) to prevent photon-assisted escape of charge carriers from the confinement.

The optoelectronic device (Fig. 4a) is fabricated in a similar way to the transport device (see Supplementary Information). Figure 4b shows an SEM image of the gate-defined monolayer $MoSe_2$ QD. The transport and optical measurements were carried out in an optical cryostat at 4 K. Current can be measured across the channel (black arrowed line), as a function of local gate voltage V_g at different silicon back gate voltage V_{BG}. Typical curves are shown in Fig. 4c: conductance plateaus are barely visible due to the long length scale of the channel leading to the centre QD, which is required to exceed the laser spot size for well-defined confinement during optical excitation. We can define $\Delta V_g = 0$ at the gate configuration where conductance is near pinch-off (blue vertical arrow in Fig. 4c for $V_{BG} = 20$ V) and confinement is expected. In contrast, confinement is absent and current can flow globally across the device at $\Delta V_g > 0.5$ V (accumulation regime), while carriers and therefore current is globally depleted across the device at $\Delta V_g < -0.1$ V (depletion regime). The observed device behaviour is in agreement with electrostatics expected in a dual-gated device design[29] (see Supplementary Information).

To demonstrate controlled localization of charged excitons, we excite the device with a laser source at $\lambda = 660$ nm and measure photoluminescence as a function of wavelength (Fig. 4d). Two emission peaks are observed corresponding to recombination processes of excitons (X) and charged excitons (X^-): the ratio of the X^- peak height over the X peak decreases as local gate voltages ΔV_g becomes more negative, due to local depletion of charged excitons as the device transits from the accumulation regime to confinement and depletion regimes respectively.

Similar behaviour in the bulk was recently observed in several, back-gate- and dopant-dependent optical studies of bulk $MoSe_2$ (refs [30,31]), the study of which gave rise to a theoretical debate as to the exact many-body nature of the charged excitonic state in the bulk when properly taking into account the interaction with the Fermi sea[30–32]. In principle, our platform could provide a handle for studying such physics in regimes ranging from mostly delocalized, bulk-like to mostly confined, potentially shedding light on the role of the different screening and interaction mechanisms involved[30–32].

At $\Delta V_g = 0$ V, the confinement potential is established, as shown by the energy of conduction band minima E_C (Fig. 5c) along the white dashed line in Fig. 4b. We then collect integrated emission signal as a function of laser position, and obtain a spatial map of emission signal in the same region as shown in Fig. 4b. Depending on the range of wavelength we choose, in which the signal is collected and integrated, we can either obtain an emission map of all excitons (Fig. 5a, collected 730–790 nm) and only charged excitons

© 2018 Macmillan Publishers Limited, part of Springer Nature. All rights reserved.

(Fig. 5b, collected 760–790 nm). The exciton emission (X) signal can be found in the entire device region (Fig. 4b) due to their charge neutral nature, independent of the electrostatic confinement potential. In contrast, as shown in Fig. 5b, the charged exciton emission (X^-) is only detected at the centre of the gate-defined confinement, as expected from our experimental design. Furthermore, we show that the confinement of charged excitons can be manipulated with a small change in local gate voltages. Figure 5d shows the phospholuminescence map for the X^- emission measured at $\Delta V_g > 0$ V, where an anti-confinement potential is created (Fig. 5e), resulting in delocalization of negatively charged excitons away from the centre of the device. By applying $\Delta V_g < 0$ V, we can also deplete charge carriers in the entire device (Fig. 5g), preventing charged exciton formation. This is confirmed by the complete suppression of the X^- emission signal (Fig. 5f).

We emphasize that the charged exciton confinement demonstrated above is realized completely by electrostatic gate control. By designing the gate structure, we can modify the confinement geometry for the charged excitons. Figure 5h shows a split-gate device with a 200 nm gap in between. At $\Delta V_g = 0$ V, we observe charged exciton emission with quasi-1D spatial span (Fig. 5i), demonstrating gate-defined 1D confinement of charged excitons. We note that the slight spatial variation of the 1D emission lines can be used as a sensitive probe to both the length and energy scale of remaining inhomogeneities in the 2DEG.

In summary, by controlling disorder in TMDs we obtained homogeneous 2DEGs that allows for excellent electrical control of both charge and excitonic degrees of freedom. By constructing gate-defined nanostructures in these TMD 2DEGs, we showed quantized conductance, tunable tunnelling barrier, and SET behaviour. Furthermore, by utilizing the large exciton binding energy of monolayer TMD, we have also demonstrated both gate-defined 0D and 1D confinement of charged excitons. Controlled manipulation of single charge carriers in engineered nanostructures that can be interfaced with photon fields can serve as a fundamental building block for novel optoelectronic devices and enable new approaches for processing and on-chip communication of classical and quantum information[33].

Received: 7 October 2016; Accepted: 15 November 2017;
Published online: 15 January 2018

References

1. Loss, D. & DiVincenzo, D. P. Quantum computation with quantum dots. *Phys. Rev. A* **57**, 120 (1998).
2. Petta, J. R. et al. Coherent manipulation of coupled electron spins in semiconductor quantum dots. *Science* **309**, 2180–2184 (2005).
3. Hanson, R., Kouwenhoven, L. P., Petta, J. R., Tarucha, S. & Vandersypen, L. M. K. Spin in few-electron quantum dots. *Rev. Mod. Phys.* **79**, 1217 (2007).
4. Jariwala, D., Sangwan, V. K., Lauhon, L. J., Marks, T. J. & Hersam, M. C. Emerging device applications for semiconducting two-dimensional transition metal dichalcogenides. *ACS Nano* **8**, 1102–1120 (2014).
5. Jariwala, D., Marks, T. J. & Hersam, M. C. Mixed-dimensional van der Waals heterostructures. *Nat. Mater.* **16**, 170–181 (2017).
6. Xiao, D., Liu, G., Feng, W., Xu, X. & Yao, W. Coupled spin and valley physics in monolayers of MoS_2 and other group-VI dichalcogenides. *Phys. Rev. Lett.* **108**, 196802 (2012).
7. Xu, X., Yao, W., Xiao, D. & Heinz, T. F. Spin and pseudospins in layered transition metal dichalcogenides. *Nat. Phys.* **10**, 343–350 (2014).
8. Kormányos, A., Zólyomi, V., Drummond, N. D. & Burkard, G. Spin-orbit coupling, quantum dots, and qubits in monolayer transition metal dichalcogenides. *Phys. Rev. X* **4**, 011034 (2014).
9. Rivera, P. et al. Valley-polarized exciton dynamics in a 2D semiconductor heterostructure. *Science* **351**, 6274 (2016).
10. Wang, Q. H., Kalantar-Zadeh, K., Kis, A., Coleman, J. N. & Strano, M. S. Electronics and optoelectronics of two-dimensional transition metal dichalcogenides. *Nat. Nanotech.* **7**, 699–712 (2012).
11. Ma, K. F. & Shan, J. Photonics and optoelectronics of 2D semiconductor transition metal dichalcogenides. *Nat. Photon.* **10**, 216–226 (2016).
12. Moody, G. et al. Electronic enhancement of the exciton coherence time in charged quantum dots. *Phys. Rev. Lett.* **116**, 037402 (2016).
13. Pioda, A. et al. Single-shot detection of electrons generated by individual photons in a tunable lateral quantum dot. *Phys. Rev. Lett.* **106**, 146804 (2011).
14. Lee, K., Kulkarnia, G. & Zhong, Z. Coulomb blockade in monolayer MoS_2 single electron transistor. *Nanoscale* **8**, 7755–7760 (2016).
15. Song, X.-X. et al. A gate defined quantum dot on the two-dimensional transition metal dichalcogenide semiconductor WSe_2. *Nanoscale* **7**, 16867–16873 (2015).
16. Song, X.-X. et al. Temperature dependence of Coulomb oscillations in a few-layer two-dimensional WS_2 quantum dot. *Sci. Rep.* **5**, 16113 (2015).
17. Mak, K. F., Lee, C., Hone, J., Shan, J. & Heinz, T. F. Atomically thin MoS_2: a new direct-gap semiconductor. *Phys. Rev. Lett.* **105**, 136805 (2010).
18. Radisavljevic, B., Radenovic, A., Brivio, J., Giacometti, V. & Kis, A. Single-layer MoS_2 transistors. *Nat. Nanotech.* **6**, 147–150 (2011).
19. Wu, Z. et al. Even–odd layer-dependent magnetotransport of high-mobility Q-valley electrons in transition metal disulfides. *Nat. Commun.* **7**, 12955 (2016).
20. Laroche, D., Gervais, G., Lilly, M. P. & Reno, J. L. 1D–1D Coulomb drag signature of a Luttinger liquid. *Science* **343**, 6171 (2014).
21. Bischoff, D. et al. Measurement back-action in stacked graphene quantum dots. *Nano Lett.* **15**, 6003–6008 (2015).
22. Payette, C. et al. Single charge sensing and transport in double quantum dots fabricated from commercially grown Si/SiGe heterostructures. *Appl. Phys. Lett.* **100**, 043508 (2012).
23. Wang, M. et al. Quantum dot behavior in bilayer graphene nanoribbons. *ACS Nano* **5**, 8769–8773 (2011).
24. Cui, X. et al. Multi-terminal transport measurements of MoS_2 using a van der Waals heterostructure device platform. *Nat. Nanotech.* **10**, 534–540 (2015).
25. Kim, K. et al. Shubnikov–de Haas oscillations of high-mobility holes in monolayer and bilayer WSe_2: Landau level degeneracy, effective mass, and negative compressibility. *Phys. Rev. Lett.* **116**, 086601 (2016).
26. Kayyalha, M., Maassen, J., Lundstrom, M., Shi, L. & Chen, Y. P. Gate-tunable and thickness-dependent electronic and thermoelectric transport in few-layer MoS_2. *J. Appl. Phys.* **120**, 134305 (2016).
27. Wang, L. et al. One-dimensional electrical contact to a two-dimensional material. *Science* **342**, 614–617 (2013).
28. van Wees, B. J. et al. Quantized conductance of point contacts in a two-dimensional electron gas. *Phys. Rev. Lett.* **60**, 848 (1988).
29. Wang, K., Payette, C., Dovzhenko, Y., Deelman, P. W. & Petta, J. R. Charge relaxation in a single-electron Si/SiGe double quantum dot. *Phys. Rev. Lett.* **111**, 046801 (2013).
30. Sidler, M. et al. Fermi polaron–polaritons in charge tunable atomically thin semiconductors. *Nat. Phys.* **13**, 255–261 (2016).
31. Scharf, B. et al. Probing many-body interactions in monolayer transition metal dichalcogenides. Preprint at https://arxiv.org/abs/1606.07101 (2016).
32. Efemkin, D. K. & MacDonald, A. H. Many-body theory of trion absorption features in two-dimensional semiconductors. *Phys. Rev. B* **95**, 035417 (2017).
33. Umansky, V., de-Picciotto, R. & Heiblum, M. Extremely high-mobility two dimensional electron gas: evaluation of scattering mechanisms. *Appl. Phys. Lett.* **71**, 683 (1997).

Acknowledgements

We thank J. Waissman and E. Lee for helpful discussions. The major experimental work was supported by AFOSR (grant FA9550-14-1-0268), DoD Vannevar Bush Faculty Fellowship (grant N00014-16-1-2825), and Samsung Electronics. K.W. acknowledges support from ARO MURI (W911NF-14-1-0247). P.K. acknowledges partial support from ONR MURI (grant N00014-15-1-2761) and the FAME Center. H.P. and M.D.L. acknowledge partial support from AFOSR MURI (FA9550-17-1-0002), NSF (PHY-1506284), and NSF CUA (PHY-1125846). K.W. and T.T. acknowledge support from the Elemental Strategy Initiative conducted by the MEXT, Japan and JSPS KAKENHI grant numbers JP26248061, JP15K21722 and JP25106006. A portion of this work was performed at the National High Magnetic Field Laboratory, which is supported by National Science Foundation Cooperative Agreement No. DMR-1157490 and the State of Florida. Nanofabrication was performed at the Center for Nanoscale Systems at Harvard, supported in part by an NSF NNIN award ECS-00335765.

Author contributions

K.W. performed the experiments and analysed the data. K.D.G., L.J., A.S., A.H., Y.Z. and G.S. performed optical measurements, K.W. and L.J. fabricated devices, K.W. and P.K. conceived the electron transport experiment. K.W., K.D.G., M.L., H.P. and P.K. conceived the optoelectronic experiment. K.W. and T.T. provided hBN crystals.

Competing interests

The authors declare no competing financial interests.

Additional information

Supplementary information is available for this paper at https://doi.org/10.1038/s41565-017-0030-x.

Reprints and permissions information is available at www.nature.com/reprints.

Correspondence and requests for materials should be addressed to P.K.

Publisher's note: Springer Nature remains neutral with regard to jurisdictional claims in published maps and institutional affiliations.

© 2018 Macmillan Publishers Limited, part of Springer Nature. All rights reserved.